High-Performance Asymmetric Li-Ion Pseudocapacitors Based on Pyroprotein Nanowebs

Se Youn Cho+,[a] Na Rae Kim+,[a] Hyoung-Joon Jin,*[a] and Young Soo Yun*[b]

Modern industrial technologies require high power and energy storage devices with long-term cycling stabilities; the electrochemical performances of these devices are mainly dependent on the active electrode materials and their energy storage mechanisms. In this study, nanoweb-structured pyroprotein nanofibers (NW-PNFs) were prepared from electrospun silk protein by pyrolysis. NW-PNFs have an open macroporous structure formed by entangled nanofibers and numerous micropores originating from the amorphous pseudographitic microstructure of the nanofibers. In addition, they possessed a large number of heteroatoms (10.3 at.% oxygen and 5.2 at.% nitrogen). These material properties led to superior Li-ion storage performances with high reversible capacity of about 1,050 mA h g^{-1} at 0.5 A g^{-1} and great cycling performance over 3,000 cycles. In particular, NW-PNFs exhibited high rate capability even at the specific current of 50 A g^{-1}, at which the high specific capacity of circa 400 mA h g^{-1} was achieved. Furthermore, asymmetric Li-ion storage devices based on NW-PNFs showed feasible electrochemical performances with a maximum specific energy of 235.7 W h kg^{-1} at 188.6 W kg^{-1} and maximum power of 21,220 W kg^{-1} at 69.6 W h kg^{-1}.

1. Introduction

Asymmetric Li-ion capacitors (ALICs) based on a combination of faradic and non-faradic electrodes can deliver high energy and great power with a long-term cycle life owing to their unique charge storage mechanism.[1–6] At the faradic electrode, Li ions can be stored in the surface and the bulk through solid-state diffusion, resulting in higher energy performances than those of supercapacitors.[1] In contrast, the charge storage of the non-faradic electrode works on the surface and near-surface of the electrode by forming electrochemical double layers through the physical adsorption and desorption of charges, leading to significantly increased rate capabilities compared with rechargeable batteries.[1,7,8] However, the different charge storage characteristics of faradic and non-faradic electrodes inevitably induce an energy and power imbalance, significantly deteriorating the electrochemical performances of ALICs.[1] To address this issue, it is required to develop a high-energy non-faradic electrode or high-power faradic electrode. Among possible alternatives, a pseudocapacitive Li-ion storage based on nanostructured active electrode materials is a feasible solution because it has been demonstrated that the surface-driven redox reaction shows fast kinetics and high capacity.[2,3,9,10]

Pyropolymers – one class of candidates for the pseudocapacitive Li-ion storage electrode – have high specific surface area containing numerous redox-active sites (such as intrinsic/extrinsic carbon defects) as well as suitable microstructure and electrical conductivity.[11–14] Pyropolymers have a few nanometer-scale pseudographitic layers that allow Li ions to be inserted/extracted rapidly into the layers in the anodic voltage region. Topological and edge defects of the poly-hexagonal carbon structure and extrinsic defects such as oxygen and nitrogen atoms can also act as redox hosts for reversible Li-ion storage.[3,15–17] The pseudocapacitive charge storage performances of pyropolymers are highly dependent on their precursor materials because the textural and surface properties and carbon microstructure are determined by the intrinsic properties of the precursor materials. Through nanostructured design with high surface-to-volume ratio, the charge storage kinetics of pyropolymers can also be immensely improved owing to the effects from nanoionics and nanoelectronics.[18–22]

In this study, nanoweb-structured pyroprotein nanofibers (NW-PNFs) – a kind of pyropolymer transformed from protein molecules – were fabricated from electrospun regenerated silk fibroin by heating in an inert gas atmosphere. The NW-PNFs had an open macroporous and microporous structure with a high specific surface area of ~575 m^2 g^{-1} and a highly disordered poly-hexagonal carbon structure with numerous defect sites. In addition, the NW-PNFs possessed a large number of oxygen and nitrogen heteroatoms (C/O and C/N ratios of 8.2 and 16.3). These unique material properties led to high electrochemical performances such as a reversible capacity of ~1,050 mA h g^{-1} and long-lasting cycle life over 3,000 repetitive galvanostatic discharge/charge cycles. In particular, the NW-PNFs showed significantly high rate capabilities; a reversible capacity of 400 mA g^{-1} was attained at a high specific current of 50 A g^{-1}. As a result, ALICs exhibiting high specific power of 80,000 W kg^{-1} at 30 W h kg^{-1} and high specific energy

[a] S. Y. Cho,+ N. R. Kim,+ Prof. H.-J. Jin
Polymer Science and Engineering
Inha University
Incheon 22212 (South Korea)
E-mail: hjjin@inha.ac.kr
[b] Prof. Y. S. Yun
Chemical Engineering
Kangwon National University
Samcheok 245-711 (South Korea)
E-mail: ysyun@kangwon.ac.kr
[+] These authors contributed to this work equally

Supporting information for this article is available on the WWW under https://doi.org/10.1002/celc.201700301

of 235.7 Wh kg^{-1} at ~188.6 W kg^{-1} were developed with a previously reported counterpart electrode based on micro-porous carbon nanosheets (MCNs).

2. Results and Discussion

The morphologies of the NW-PNFs were observed from the field emission scanning electron microscopy (FE-SEM) image (Figure 1(a)), which shows a macroporous nanoweb structure
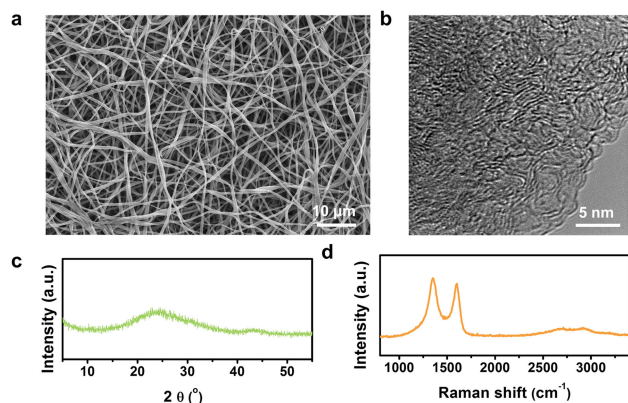

Figure 1. Morphologies and microstructural properties of NW-PNFs. a) FE-SEM image, b) FE-TEM image, c) XRD pattern, and d) Raman spectrum of NW-PNFs..

composed of high aspect ratio nanofibers with diameters of ~300 nm and lengths of several micrometers. Further magnified FE-SEM image and FE-TEM image support the diameter of the nanofibers [Figure S1]. The high-resolution field emission transmission electron microscopy (FE-TEM) image of the NW-PNFs provides information about their microstructure, which is an amorphous structure without long-range ordering [Figure 1(b)]. The observed microstructural result is supported by the X-ray diffraction (XRD) pattern in which very broad graphite (002) and (100) peaks are found at ~24° and 43°, respectively, confirming the amorphous structure consisting of a pseudographitic structure [Figure 1(c)].[12] In contrast, the Raman spectrum of the NW-PNFs reveals clear carbon-induced D and G bands at ~1,350 and ~1,600 cm^{-1}, respectively [Figure 1(d)]. The D and G bands originate from the intrinsic phonon mode of the infinite aromatic ring (with A$_{1g}$ symmetry) that is activated by the structural disorder and the hexagon carbon structure related to the E$_{2g}$ vibration mode of the sp^2-hybridised C atoms.[23] Therefore, from these Raman bands, it is confirmed that an aromatic poly-hexagonal carbon structure is well-developed. In addition, the D to G intensity ratio (I$_D$/I$_G$ ≈ 1.1) indicates an approximate size for the hexagonal carbon structure whose lateral size is calculated as a few nanometers.[24–26] Meanwhile, unlike the clear D and G bands, a weak 2D band centered at ~2,690 cm^{-1} was exhibited, indicating that there is poor three-dimensional carbon ordering, agreeing with the FE-TEM and XRD results.[27,28]

The surface properties of the NW-PNFs were characterized by X-ray photoelectron spectroscopy (XPS), as shown in Figure 2(a–c). In the C 1s spectra, sp^2 C=C bonding was
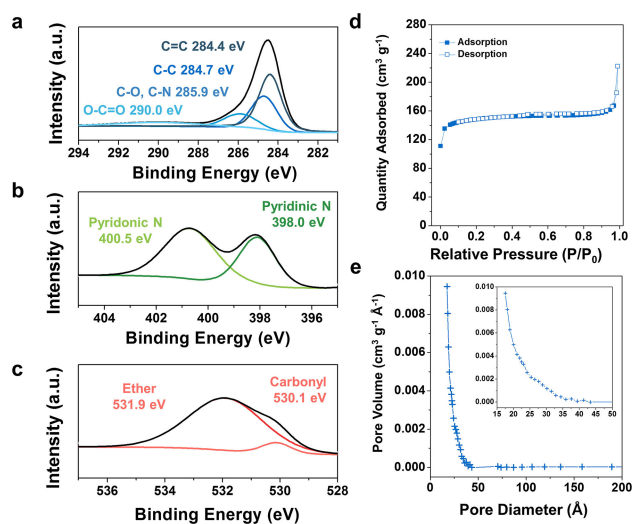

Figure 2. Surface properties and pore structure of NW-PNFs. XPS a) C 1s, b) N 1s, and c) O 1s spectra of NW-PNFs. d) Nitrogen adsorption and desorption isotherms, and e) pore size distribution data of NW-PNFs. Inset in (e): Magnified portion of the pore size distribution curve.

identified at 284.4 eV and considerable sp^3 C–C bonding was also observed at 284.7 eV, indicating the presence of numerous topological defects in the hexagonal carbon domains [Figure 2(a)].[24] Extrinsic defects such as C–O and C–N bonding at 285.9 eV and O-C=O bonding at 290.0 eV were also confirmed.[29] In the N 1s spectrum, the nitrogen atoms were pyridinic N (398.0 eV) and pyridonic N (400.5 eV) [Figure 2(b)]. The oxygen groups were primarily ether bonding at 531.9 eV and carbonyl structures at 530.1 eV in the O 1s spectrum [Figure 2(c)].[30] The C/O and C/N ratios of NW-PNFs were 8.2 and 16.3, respectively.

The pore structure of NW-PNFs was characterized by nitrogen adsorption and desorption isotherm curves, shown in Figure 2(d) and 2(e). The adsorption curve shows a dramatic increase in the quantity of nitrogen adsorbed for relative pressure below 0.1, indicating a large amount of monolayer adsorption [Figure 2(d)]. This could be induced by adsorption on the surface of disordered hexagonal carbon layers because their poor stacking ordering allows nitrogen molecules to permeate. Considering that the kinetic diameter of nitrogen molecules (~4 Å) is larger than that of the Li ion, the extensive monolayer adsorption area can be an electrochemically active surface area for charge storage.[31] On the other hand, nitrogen molecules were slightly adsorbed for relative pressure between 0.1 and 0.9, suggesting poor mesopore development. Pore size distribution data support this result, as shown in Figure 2(e). Most pores are distributed in the small diameter region (below 3 nm) and there is little pore volume in pores with diameters between 3 and 50 nm. At relative pressure close to 1, the adsorption curve rapidly rises and the desorption curve exhibits

no hysteresis, indicating a large amount of nitrogen adsorption without the capillary condensation associated with pores, which suggests the presence of macroporous structures. From these nitrogen adsorption and desorption isotherm curves, it is confirmed that NW-PNFs have a hybrid microporous and macroporous structure corresponding to an IUPAC type-I and -IV hybrid shape. The specific surface area calculated from Brunauer-Emmett-Teller (BET) theory is $\sim 575\ m^2 g^{-1}$ in which the micropore surface area corresponds to $\sim 450\ m^2 g^{-1}$.

The electrochemical performance of NW-PNFs was tested in an electrolyte of $LiPF_6$ dissolved in ethylene carbonate (EC) and dimethyl carbonate (DMC) mixture ($v:v = 1:1$) solution in the voltage window between 0.01 and 2.7 V vs. Li^+/Li, as shown in Figure 3. The galvanostatic discharge/charge profiles of NW-PNFs at a specific current rate of $0.5\ A g^{-1}$ show continuous voltage decrease/increase with Li-ion insertion/extraction, indicating charge storage behavior by a solid solution reaction with no phase transition [Figure 3(a)]. The first discharge capacity is abnormally high ($\sim 2,980\ mAh g^{-1}$), of which a considerable value (approximately $1,930\ mAh g^{-1}$) originates from irreversible reactions such as solid-electrolyte-interface (SEI) layer formation. The presence of large side reactions indicates that NW-PNFs have an extensive electrochemically active surface area. The first cyclovoltammogram (CV) of NW-PNFs shows a clear reduction peak at 0.75 V, supporting the SEI formation reaction [Figure 3(b)]. The reversible capacity of NW-PNFs corresponds to $\sim 1,050\ mAh g^{-1}$ and most of the capacity originates from the low voltage region (below 1.5 V) [Figure 3(a) and 3(b)]. The high reversible Li-ion storage capacity could be caused by the large number of intrinsic/extrinsic defect sites on the NW-PNFs. In addition, NW-PNFs exhibited significantly high rate capabilities at specific current rates from 0.5 to $50\ A g^{-1}$, as shown in Figure 3(c) and 3(d). While the specific capacities gradually decreased with increasing current rates, high specific capacities of ~ 605, ~ 555, ~ 495, and $\sim 400\ mAh g^{-1}$ at 5, 10, 20, and $50\ A g^{-1}$, respectively, were observed at low redox voltage [Figure 3(c)]. The corresponding capacitance values at different current densities were added in Table S1. Furthermore, when the specific current rates returned to the initial value of

$0.5\ A g^{-1}$ after continuous cycling by gradually increasing the current rates to $50\ A g^{-1}$, the NW-PNFs successfully recovered their initial capacity, indicating good reversibility [Figure 3(d)]. Electrochemical impedance spectroscopy (EIS) results show that the initial charge transfer resistance (R_{ct}) of NW-PNFs exceeds 90 Ω, which is considerably high value. However, the value is significantly reduced after Li-ion insertion, indicating that kinetics of Li ion chemisorption can be accelerated with charge storage [Figure S2]. Cycling performances of NW-PNFs were tested at $1\ A g^{-1}$ over 3,000 cycles, which shows a steady increase of the specific capacity with cycling [Figure 3(e)]. The early specific capacities of $\sim 710\ mAh g^{-1}$ reached the ~ 1.3-fold higher value of $\sim 920\ mAh g^{-1}$ while maintaining their charge storage profiles after 3,000 cycles. Similar phenomena were observed in graphene-based anode materials and this could be caused by an increase in the electrochemical active surface area of NW-PNFs with cycling.

The feasibility of NW-PNFs for energy storage was confirmed by assembling ALICs with MCNs in which the anode and cathode were pre-cycled for 10 cycles, and the onset voltage was set at 1.5 V vs. Li^+/Li.[32] The electrochemical performances of MCNs can be confirmed from Figure S3. The schematic image shown in Figure S4 depicts the charge storage behaviors of the NW-PNF//MCN ALICs. While the NW-PNF anode works in the voltage range 0.01–1.5 V, the MCN cathode operates in the voltage region 1.5–4.51 V. As a result, the ALICs have a large working voltage of 4.5 V. Electrochemical performances of the ALICs were tested by CV and galvanostatic charge/discharge [Figure 4]. At a sweep rate of $5\ mV s^{-1}$, the CV curves of the NW-PNF//MCN ALICs show a rectangular shape, indicating surface-driven charge storage behaviors [Figure 4(a)]. The initial shape of the CV curves (with large area) was maintained with increasing sweep rates, showing high power and energy performances of the ALICs. The galvanostatic charge/discharge profiles also show the shape of an isosceles triangle at different current rates, coinciding with the CV data [Figure 4(b)]. The specific capacitance values of the ALICs were added in Table S2. Equivalent series resistance of the NW-PNF//MCN ALICs was around 60 Ω, which is reduced by ~ 35 Ω with repetitive cycling
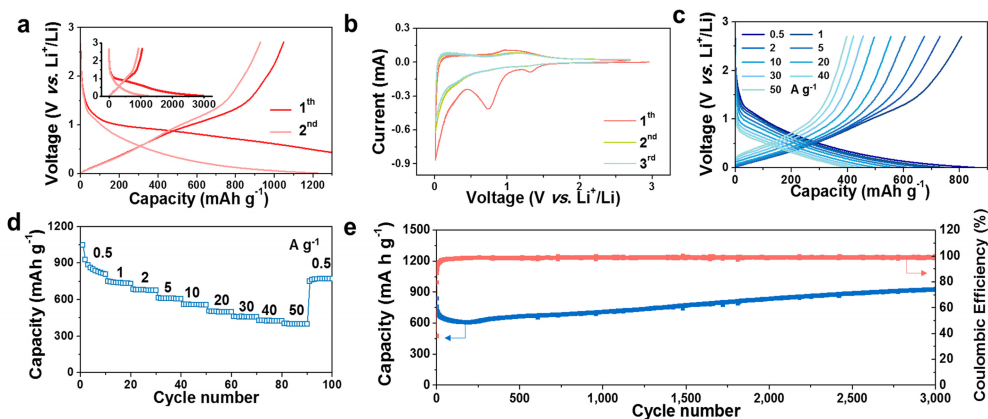

Figure 3. Electrochemical properties of NW-PNFs in an electrolyte 1 M $LiPF_6$ dissolved in EC/DMC ($v:v = 1:1$) over a voltage window between 0.01 to 2.7 V vs. Li^+/Li. a) Glavanostatic discharge and charge profiles of NW-PNFs at $0.5\ A g^{-1}$. b) Cyclovoltammograms at $0.1\ mV s^{-1}$. c,d) Rate capabilities at various current densities from 0.5 to $50\ A g^{-1}$. e) Cycling performance data over 3000 cycles at $1\ A g^{-1}$.
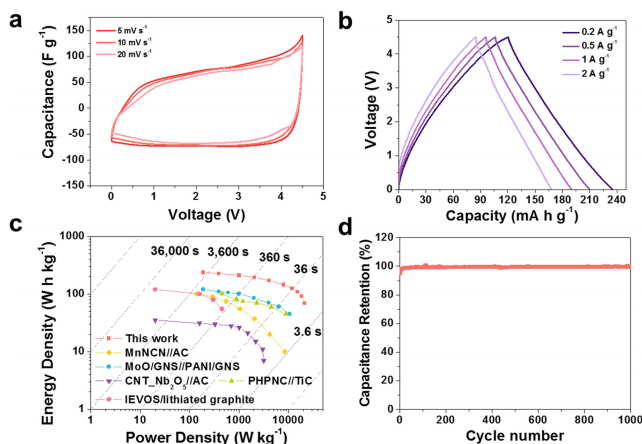
Figure 4. Electrochemical performances of ALICs assembled with NW-PNF and MCN as an anodes and cathodes, respectively, in the voltage window 0–4.5 V in 1 M LiPF$_6$ in 1:1 (v:v) EC/DMC. a) CV curves at scan rates of 5, 10, and 20 mV s^{-1}. b) Galvanostatic charge/discharge profiles at various current densities from 0.2 to 2 A g^{-1}. c) Ragone plots of several ALICs based on NW-PNF//MCN, MnNCN//AC, MoO/GNS//PANI/GNS, CNT_Nb$_2$O$_5$//AC, PHPNC//TiC and IEVOS//lithiated graphite. d) Cycling performance over 1000 cycles at a current density of 1 A g^{-1}.

[Figure S5]. The Ragone plot of the NW-PNF//MCN ALICs is displayed with previously reported results to compare their energy and power characteristics in Figure 4(c). The NW-PNF//MCN ALICs show a maximum energy of ~235.7 Wh kg^{-1} at ~188.6 W kg^{-1} and a maximum power of 21,220 W kg^{-1} at 69.6 Wh kg^{-1}, which are higher than those of reported devices based on MnNCN//AC,[33] MoO/GNS//PANI/GNS,[34] CNT_Nb$_2$O$_5$//AC,[35] PHPNC//TiC,[36] and IEVOS//lithiated graphite.[37] Moreover, stable cycling behaviors with capacity retention of ~80% were achieved after 1,000 cycles, demonstrating the practicability of these energy storage devices [Figure 4(d)].

3. Conclusions

NW-PNFs were fabricated from electrospun regenerated silk fibroin by pyrolysis and their electrochemical performances for Li-ion storage were tested in the cathodic voltage region. NW-PNFs have a nanoweb architecture composed of high aspect ratio carbonaceous nanofibers with an amorphous microstructure exhibiting a dual macroporous and microporous structure. Their specific surface area was ~575 m^2 g^{-1} and micropores formed the major contribution (~450 m^2 g^{-1}). In addition, the NW-PNFs contained numerous oxygen and nitrogen heteroatoms (C/O and C/N ratios of 8.2 and 16.3 at%, respectively). Consequently, significantly high energy and kinetic performances such as reversible capacities of ~1,050 mA h g^{-1} and 400 mA h g^{-1} at 0.5 and 50 A g^{-1}, respectively, and long-term cycling performances over 3000 cycles were achieved. NW-PNF//MCN ALICs showed long-term cycling behaviors with capacity retention of 80% after 1,000 cycles as well as high energy and power performances, such as a maximum energy of ~235.7 Wh kg^{-1} at ~188.6 W kg^{-1} and a maximum power of 21,220 W kg^{-1} at 69.6 Wh kg^{-1}.

Experimental Section

Preparation of NW-PNFs

Cocoons from *B. mori* silkworms (Uljin Farm, South Korea) were boiled for 25 min in an aqueous solution containing 0.02 M Na$_2$CO$_3$ (99%; OCI Co., South Korea) and rinsed thoroughly with deionized water to extract the glue-like sericins and other impurities (i.e., a degumming process).[33] After drying at room temperature for 3 d, the resulting fibrous silk fibers (silk fibroin) were dissolved in an aqueous solution of 9.3 M LiBr (99%; Sigma-Aldrich, St. Louis, MO, USA) at 60 °C for 6 h. The silk fibroin solution was dialyzed in water using a Slide-a-Lyzer dialysis cassette (MWCO 3500; Pierce) for 2 d. The final concentration of the silk fibroin in the aqueous solution was approximately 8 wt%.

Electro-spinning was employed to fabricate the silk fibroin nano-webs. Following freezing for 6 h at −80 °C, the frozen silk fibroin solution was subjected to lyophilization at −50 °C and 0.045 mbar for 72 h. The resulting cylindrical silk fibroin sponge was dissolved in 98% formic acid (Junsei Chemical Co. Japan) with mild stirring for 1 d under ambient conditions. The mass fraction of silk protein (relative to formic acid) was 10%. The solution was filled in a plastic syringe and the syringe was connected to a metal needle with a diameter of 0.514 mm. A rotating disk surrounded by copper foil with an angular velocity of 1500 rpm was placed 15 cm from the needle and used to collect the electrospun silk fibroin nanofibers. A potential of 15 kV was applied between the metal needle and the copper foil. The electro-spinning process was performed at room temperature with a relative humidity of less than 40%.

The as-prepared silk fibroin nanowebs were heated to 800 °C under controlled heating schedules in a tubular furnace with an argon atmosphere (minimum purity, 99.999%; gas flow, 100 cm^3 min^{-1}). The carbonization process was as follows. The silk nanowebs were rapidly heated to 150 °C and this temperature was maintained for 2 h to remove residual water. After heating at a rate of 10 °C min^{-1}, the samples were maintained at 350 °C for 3 h to induce the formation of the conjugated carbon structure. The resultant was heated to 800 °C at a rate of 5 °C min^{-1} followed by a two-hour isotherm at that temperature. The resulting NW-PNFs were stripped off from the Cu foil and used as an electrode for Li-ion storage.

Electrochemical Characterization

Electrochemical performances of NW-PNFs, MCNs, and their ALICs were characterized using a Wonatech automatic battery cycler and CR2032-type coin cells. For the half-cell experiments, coin cells were assembled in a glove box filled with argon using NW-PNFs or MCNs as the working electrode and metallic Li foil as the reference and counter electrodes. LiPF$_6$ (1 M; Aldrich, 99.99%) was dissolved in a solution of EC/DMC mixture (v:v = 1:1) solution and used as the electrolyte for Li-ion storage. A glass microfiber filter (GF/F, Whatman) was used as the separator. NW-PNFs were punched into discs 1/2″ in diameter and used as the working electrode without a binder, Super P, or substrate, while the MCN-based counter electrode was prepared by mixing the active material (80 wt%) with conductive carbon (10 wt%) and polyvinylidene fluoride (10 wt%) in *N*-methyl-2-pyrrolidone. The resulting slurry was uniformly applied on Cu or Al foil. The electrodes were dried at 120 °C for 2 h. For the full-cell experiments, coin cells were assembled in a glove box filled with argon using NW-PNFs and MCNs as the anode and cathode, respectively. Loading densities of the active materials were about 0.5 mg cm^{-2} and 2 mg cm^{-2} for NW-PNFs and MCNs, respectively. The ALICs used the same electrolyte and separator materials as the half-cells. EIS tests were performed at room temperature in the frequency range of 100 kHz

to 0.1 Hz using an impedance analyzer (ZIVE SP2, WonATech). The specific capacitance (C) was determined from the galvanostatic measurements using the following equation [Eq. (1)]:[29]

$$C = \frac{4 I_{cons}}{m \, dV/dt} \tag{1}$$

where I_{cons} is the discharge (constant) current, m is the total mass of active materials, and dV/dt was calculated from the slope of the discharge curve over the range from $V = V_{max}$ (the voltage at the beginning of discharge) to $V = 1/2 V_{max}$. The energy density (E) and power density (P) values were calculated using the following equations [Eqs. (2), (3)]:

$$E = I_{cons} \int_{t=0}^{t=t} V(t) \, dt \tag{2}$$

$$P = \frac{E}{t} \tag{3}$$

Where I_{cons} is the discharge (constant) current, t (second) is the discharge time, m (gram) is the total mass of active materials, V (volt) is the potential range during discharge.[39]

Characterization

Morphologies of NW-PNFs were examined by FE-SEM(S-4300, Hitachi, Japan) and FE-TEM (JEM2100F, JEOL, Japan). Raman spectra were recorded using a continuous-wave linearly polarized laser (514.5 nm, 2.41 eV, 16 mW). The laser beam was focused by a 100× objective lens, resulting in a spot with diameter of ~1 μm. Three scans were used to collect each spectrum with an acquisition time of 10 s. XRD (Rigaku DMAX 2500) analysis was performed using Cu-K_α radiation ($\lambda = 0.154$ nm) at 40 kV and 100 mA. The chemical properties of the NW-PNFs were examined by XPS (PHI 5700 ESCA, USA) using monochromatic Al-K_α radiation ($h\nu = 1{,}486.6$ eV). The pore structures of NW-PNFs were analyzed using nitrogen adsorption and desorption isotherms recorded on a surface area and porosimetry analyzer (Tristar, Micromeritics, USA) at $-196\,^\circ$C. The surface area was calculated according to the BET theory.

Acknowledgements

Conflict of Interest

The authors declare no conflict of interest.

[1] M. R. Lukatskaya, B. Dunn, Y. Gogotsi, *Nat. Commun.* **2016**, *7*, 12647.
[2] S. W. Lee, N. Yabuuchi, B. M. Gallant, S. Chen, B.-S. Kim, P. T. Hammond, Y. Shao-Horn, *Nat. Nanotechnol.* **2010**, *5*, 531–537.
[3] Y. S. Yun, D.-H. Kim, S. J. Hong, M. H. Park, Y. W. Park, B. H. Kim, H.-J. Jin, K. Kang, *Nanoscale* **2015**, *7*, 15051–15058.
[4] H. Kim, M.-Y. Cho, M.-H. Kim, K.-Y. Park, H. Gwon, Y. Lee, K. C. Roh, K. Kang, *Adv. Energy Mater.* **2013**, *3*, 1500–1506.
[5] H. Kim, K.-Y. Park, M.-Y. Cho, M.-H. Kim, J. Hong, S.-K. Jung, K. C. Roh, K. Kang, *ChemElectroChem* **2014**, *1*, 125–130.
[6] B. Z. Jang, C. Liu, D. Neff, Z. Yu, M. C. Wang, W. Xiong, A. Zhamu, *Nano Lett.* **2011**, *11*, 3785–3791.
[7] Y. Zhu, S. Murali, M. D. Stoller, K. J. Ganesh, W. Cai, P. J. Ferreira, A. Pirkle, R. M. Wallace, K. A. Cychosz, M. Thommes, D. Su, E. A. Stach, R. S. Ruoff, *Science* **2012**, *332*, 1537–1541.
[8] C. Merlet, B. Rotenberg, P. A. Madden, P.-L. Taberna, P. Simon, Y. Gogotsi, M. Salanne, *Nat. Mater.* **2012**, *11*, 306–310.
[9] H. Kim, H.-D. Lim, S.-W. Kim, J. Hong, D.-H. Seo, D. Kim, S. Jeon, S. Park, K. Kang, *Sci Rep* **2013**, *3*, 1506.
[10] W. Gu, N. Peters, G. Yushin, *Carbon* **2013**, *53*, 292–301.
[11] G. M. Jenkins, K. Kawamura, Polymeric Carbons-Carbon Fibre, Glass and Char, Cambridge University Press, London, New York, Melbourne, **1976**.
[12] S. Y. Cho, Y. S. Yun, S. Lee, D. Jang, K.-Y. Park, J. K. Kim, B. H. Kim, K. Kang, D. L. Kaplan, H.-J. Jin, *Nat. Commun.* **2015**, *6*, 7145.
[13] Y. S. Yun, Y. H. Kim, M. Y. Song, N. R. Kim, K. Ku, J. S. An, K. Kang, H, J. Choi, H.-J. Jin, *J. Power Sources* **2016**, *331*, 507–514.
[14] H. J. An, N. R. Kim, M. Y. Song, Y. S. Yun, H.-J. Jin, *J. Ind. Eng. Chem.* **2017**, *45*, 223–228.
[15] J. Hong, M. Lee, B. Lee, D.-H. Seo, C. B. Park, K. Kang, *Nat. Commun.* **2014**, *5*, 5335.
[16] Y. Liu, V. I. Artyukhov, M. Liu, A. R. Harutyunyan, B. I. Yakobson, *J. Phys. Chem. Lett.* **2013**, *4*, 1737–1742.
[17] Y. S. Yun, K.-Y. Park, B. Lee, S. Y. Cho, Y.-U. Park, S. J. Hong, B. H. Kim, H. Gwon, H. Kim, S. Lee, Y. W. Park, H.-J. Jin, K. Kang, *Adv. Mater.* **2015**, *27*, 6914–6921.
[18] S. L. Candelaria, Y. Shao, W. Zhou, X. Li, J. Xiao, J.-G. Zhang, Y. Wang, J. Liu, J. Li, G. Cao, *Nano Energy* **2012**, *1*, 195–220.
[19] Z. Li, D. Wu, Y. Liang, R. Fu, K. Matyjaszewski, *J. Am. Chem. Soc.* **2014**, *136*, 4805–4808.
[20] Z. Li, L. Li, Z. Li, H. Liao, H. Zhang, *Electrochim. Acta* **2016**, *222*, 990–998.
[21] W. Lu, C. M. Lieber, *Nat. Mater.* **2007**, *6*, 841–850.
[22] J. Maier, *Nat. Mater.* **2005**, *4*, 805–815.
[23] M. Y. Song, S. Y. Cho, N. R. Kim, S.-H. Jung, J.-K. Lee, Y. S. Yun, H.-J. Jin, *Carbon* **2016**, *108*, 274–282.
[24] A. C. Ferrari, J. Robertson, *Phys. Rev. B* **2000**, *61*, 14095.
[25] F. Tuinstra, J. L. Koenig, *J. Chem. Phys.* **1970**, *53*, 1126–1130.
[26] L. G. Cancado, K. Takai, T. Enoki, M. Endo, Y. A. Kim, H. Mizusaki, A. Jorio, L. N. Coelho, R. Magalhães-Paniago, M. A. Pimenta, *Appl. Phys. Lett.* **2006**, *88*, 163106.
[27] M. S. Dresselhaus, A. Jorio, M. Hofmann, G. Dresselhaus, R. Saito, *Nano Lett.* **2010**, *10*, 751–758.
[28] P. Lespade, A. Marchand, M. Couzi, F. Cruege, *Carbon* **1984**, *22*, 375–385.
[29] Y. S. Yun, G. Yoon, K. Kang, H.-J. Jin, *Carbon* **2014**, *80*, 246–254.
[30] N. R. Kim, Y. S. Yun, M. Y. Song, S. J. Hong, M. Kang, C. Leal, Y. W. Park, H.-J. Jin, *ACS Appl. Mater. Interfaces* **2016**, *8*, 3175–3181.
[31] N. Mehio, S. Dai, D. Jiang, *J. Phys. Chem. A* **2014**, *118*, 1150 − 1154.
[32] Z. Weng, F. Li, D.-W. Wang, L. Wen, H.-M. Cheng, *Angew. Chem. Int. Ed.* **2013**, *52*, 3722–3725.
[33] C. Liu, C. Zhang, H. Fu, X. Nan, G. Cao, *Adv. Energy Mater.* **2017**, *7*, 1601127.
[34] W. Liu, J. Li, K. Feng, A. Sy, Y. Liu, L. Lim, G. Lui, R. Tjandra, L. Rasenthiram, G. Chiu, A. Yu, *ACS Appl. Mater. Interfaces* **2016**, *8*, 25941 − 25953.
[35] X. Wang, G. Li, Z. Chen, V. Augustyn, X. Ma, G. Wang, B. Dunn, Y. Lu, *Adv. Energy Mater.* **2011**, *1*, 1089–1093.
[36] H. Wang, Y. Zhang, H. Ang, Y. Zhang, H. T. Tan, Y. Zhang, Y. Guo, J. B. Franklin, X. L. Wu, M. Srinivasan, H. J. Fan, Q. Yan, *Adv. Funct. Mater.* **2016**, *26*, 3082–3093.
[37] N. Xu, X. Ma, M. Wang, T. Qian, J. Liang, W. Yang, Y. Wang, J. Hu, C. Yan, *Electrochim. Acta* **2016**, *203*, 171–177.
[38] Y. S. Yun, S. Y. Cho, J. Shim, B. H. Kim, S.-J. Chang, S. J. Baek, Y. S. Huh, Y. Tak, Y. W. Park, S. Park, H.-J. Jin, *Adv. Mater.* **2013**, *25*, 1993–1998.
[39] J. B. Goodenough, Y. Kim, *J. Power Sources* **2011**, *196*, 6688–6694.